

Temperature and number density measurement in non-uniform supersonic flowfields undergoing mixing using toluene PLIF thermometry

Mirko Gamba¹ · Victor A. Miller² · M. Godfrey Mungal³ · Ronald K. Hanson²

Received: 17 May 2014 / Accepted: 7 May 2015 / Published online: 3 June 2015
© Springer-Verlag Berlin Heidelberg 2015

Abstract Single-excitation, dual-band-collection toluene planar laser-induced fluorescence (PLIF) is used to measure temperature and number density (or partial pressure) fields in non-uniform supersonic complex flows in the presence of mixing and compressibility. The study provides a quantitative evaluation of the technique in transverse jets in supersonic crossflow (JISCF). It is found that toluene PLIF is highly effective in visualizing the structure of supersonic flows and that temperature can be accurately inferred with acceptable signal-to-noise ratios (of order 30) even when mixing occurs. The technique was applied to several JISCFs that differ by jet fluid properties with resulting different structures. In the presence of compressibility and mixing, it is found that the PLIF signal is non-unique, a feature that is used to identify the mixing region of the transverse jet. Measurement errors due to camera registration errors have also been quantified. Because of the complexity of the flowfield, it is found that minute misalignment (<0.1 pixels) between the two PLIF images can introduce measurable errors on the order of tens of Kelvins and significant errors in temperature gradients.

1 Introduction

Tracer-based planar laser-induced fluorescence (PLIF) imaging is now a well-established technique for the

visualization and quantification of many flow properties, including scalar concentration and temperature measurements, and it has been long used in both low- and high-speed flows. PLIF imaging based on a variety of tracers has been considered through the literature [1]. Historically, acetone and 3-pentanone [2, 3] have been widely used for scalar and temperature imaging, and more recently, naphthalene [4, 5], krypton [6], 1-methylnaphthalene [7], and anisole [8] have been utilized in a variety of applications.

Toluene has been identified as a versatile candidate for PLIF studies owing to its large fluorescence quantum yield and strong temperature sensitivity [9–13]. Toluene PLIF has found many applications for the study of mixing, especially in internal combustion engine studies [10, 12, 14–17] where the strong oxygen quenching [18] has been used to obtain a direct measurement of air/fuel ratio [1, 12, 19]. Some of the challenges (particularly related to pressure effects) on the use of toluene for fuel/air ratio measurements have also been identified [12, 15, 20, 21]. The properties of oxygen quenching on fluorescence have also been exploited for a direct measure of oxygen concentration in both single-tracer [22] and dual-tracer [23] configurations. Furthermore, because of the relatively large fluorescence quantum yield, toluene PLIF has also been successfully used for high-framing-rate imaging configurations where laser pulse energies are typically limited [14, 20, 24].

Toluene PLIF has proven to be a particularly robust approach for temperature measurements. Both single- and dual-band-detection schemes have been proposed [10, 13] and applied [16, 25–29]. Its use as a thermometry technique stems from the strong temperature dependence of the integrated fluorescence quantum yield and the temperature-induced red shift of the spectral fluorescence

✉ Mirko Gamba
mirkog@umich.edu

¹ University of Michigan, Ann Arbor, MI, USA

² Stanford University, Stanford, CA, USA

³ Santa Clara University, Santa Clara, CA, USA

[10–13]. A single-band-detection scheme takes advantage of the temperature dependence: the tracer is excited with a suitable laser (for toluene, 266 and 248 nm are common) and the resulting fluorescence is collected over the full spectrum. For uniform and isobaric (or of known pressure variation) situations, the collected fluorescence can be directly related to the tracer's temperature. On the contrary, the dual-band-detection scheme primarily relies on the temperature-induced red shift: following single-wavelength excitation, fluorescence is collected over two different spectral regions (for example on two different detectors or cameras, or on the same one by splitting the imaging region) and the ratio between the collected portion is related directly to temperature. The advantage of this second approach is that pressure and tracer number density dependence does not come into play in the temperature reconstruction procedure. Because of this, dual-collection strategies are typically preferred in complex flowfields, such as in supersonic flows.

In some of our previous work on toluene PLIF thermometry, we optimized and verified the dual-band-collection thermometry strategy for the study of supersonic flows dominated by shock waves but with uniform tracer distributions [26]. In this study, we extend the use of the method to study the temperature field and mixing in non-uniform supersonic flowfields. In particular, we apply the method to the study of mixing of the transverse jet in supersonic crossflow (JISCF). The transverse jet in crossflow (JICF) is a canonical flow with relevance to many engineering applications. The JICF system arises when fluid is injected perpendicularly to a crossflow. In the supersonic case (JISCF), both the jet and the crossflow might be supersonic. Recent reviews [30, 31] on the general properties of JICF give an up-to-date summary of their current understanding.

In this study, we evaluate the two-color toluene PLIF thermometry technique applied to a JISCF formed by sonic injection of different room temperature fluids into an elevated temperature supersonic nitrogen crossflow seeded with toluene. Similar to our previous work [26], we use single-excitation (at 266 nm), dual-band detection toluene PLIF thermometry to locally measure the fluid temperature and tracer number density, from which a measure of mixing is inferred. Dual-band detection is carried out with two imaging systems equipped with a high-pass filter with a cutoff wavelength near 305 nm and a band-pass filter centered at 280 ± 10 nm, respectively. The mapping function between temperature and the ratio of the two PLIF images is constructed from the known spectroscopy of toluene [10–13] without any in-situ calibration. Although the spectroscopy of toluene is not affected by the different fluids used here, the resulting temperature fields are different because of different thermophysical properties and the

somewhat different fluid dynamic processes, which will be evaluated in a later publication.

Here we evaluate how toluene PLIF thermometry can capture the complex flowfield in these JISCFs under different conditions. We also consider cases where oxygen quenching is present by injecting air into the nitrogen crossflow. After we first summarize the toluene PLIF thermometry technique and the experimental methods used in this study, we present some representative data for hydrogen, argon and air injection. Then, we evaluate the accuracy of the technique and we construct a zero-dimensional, isobaric mixing model to describe the properties of toluene PLIF in these supersonic flows. We also evaluate the precision (estimated from a local measure of the spatial signal-to-noise ratio) of the measurements, as well as measurement errors arising from image registration errors, which are here found to have a significant role on the accuracy of the measurements and on how the flowfield is rendered. In this regard, we evaluate the impact of image registration errors from numerical experiments using data from large eddy simulations (LES) of a non-reacting JISCF [32] constructed to replicate some of the methods used in the experiments.

2 Toluene PLIF thermometry in non-homogenous compressible flows

A complete description of the approach, its optimization and an assessment of its accuracy in uniformly seeded flows has been presented by [26], and only a brief overview is given here to aid discussion of the mixing studies presented here.

2.1 Oxygen-free environments

In the dual-collection configuration, two spectral bands are imaged simultaneously with independent imaging systems following single-wavelength excitation (at 266 nm in this work). For each view i ($i = 1, 2$), at a given excitation wavelength, the collected LIF signal $S_{f,i}$ (in the weak excitation limit) depends on the number of incident photons $E/h\nu$ (where E and ν are the energy and frequency of the excitation laser, respectively), its absorbed fraction $n\sigma$ (where n and σ are the number density and absorption cross section of the absorbing species, respectively), the fraction of photons emitted as fluorescence over the fluorescence spectrum ϕ (which is the spectral fluorescence quantum yield), and the fraction collected by the imaging system $\tau\eta$ (which includes any efficiency of the collection system, η , and the spectral transmission of any optical filter used, τ):

$$S_{f,i}(T; p) = \frac{E}{h\nu} n\sigma(T) \int_{\Omega_\tau} \tau_i(\lambda)\phi(\lambda, T; p)\eta_i(\lambda)d\lambda \quad (1)$$

Integration is carried out over the spectral bandwidth of the optical filter Ω_τ . Here $S_{f,i}$ is intended per unit volume of the probed region.

The absorption cross section and spectral fluorescence quantum yield (FQY) of toluene have been measured as a function of temperature in previous studies [10, 11, 13, 20]. Pressure dependence has also been documented [20, 28]. In particular, for partial pressure around 10–20 mbar (which is the range of saturation pressure of toluene around room temperature), the integrated FQY is pressure independent for total pressure larger than 0.8 bar for 266-nm excitation at room temperature [20]. In compressible flow applications where large variation of pressure can exist, any pressure dependence is generally unwanted, and conditions of operation must take pressure dependence into consideration or avoid it. In the current work, the flow conditions have been selected to operate in the pressure-independent regime, although the large variation of pressure associated with the traverse jet in supersonic crossflow could invalidate this assumption locally (discussed further below).

According to the following relation, the ratio between the LIF signal collected over the two bands depends only on the local temperature:

$$R(T) = \frac{S_{f,1}(T)}{S_{f,2}(T)} = \frac{\int_{\Omega_{\tau,1}} \tau_1(\lambda) \phi(\lambda, T) \eta_1(\lambda) d\lambda}{\int_{\Omega_{\tau,2}} \tau_2(\lambda) \phi(\lambda, T) \eta_2(\lambda) d\lambda} \quad (2)$$

This conclusion is correct only if pressure effects on fluorescence are absent and if the red shift is due only to changes in temperature. In this case, the LIF ratio is independent of the local number density of the tracer. Thus, temperature can be extracted from a measure of the LIF ratio even if mixing occurs.

Koban [10] and Miller et al. [26] identified the BP280/WG305 pair as the optimal combination of filters for the range of temperature relevant to compressible flow applications. This filter combination is also used in the current study. With this filter pair, we integrate each term in Eq. 2 to find a relation between temperature and R that does not require any further calibration step. Because the ratio is constructed from the ratio of measurements with different cameras (or in general, detectors) with different properties (i.e., quantum efficiency, gains, $f/\#$, etc.), the only required in-situ calibration is to express $R(T)$ relative to the value at a known reference temperature (here taken to be room temperature, $T_{\text{ref}} = 295 \text{ K}$) i.e., $R(T)/R(T_{\text{ref}})$. The resulting normalized ratio is therefore a unique function of temperature and does not depend on any of the details of the imaging system. In practice, this normalization is carried out by performing an initial imaging of the uniformly seeded field at room temperature and it is included as part of the sheet uniformity correction step that is required. The

resulting calibration curves using the BP280/WG305 filter pair are given in [26] with spectroscopy data courtesy of [18].

2.2 Flows with oxygen

The results described above strictly apply for the case of an oxygen-free environment. For the test carried out in this work, our crossflow is nitrogen seeded with toluene, while we inject different fluids, including air. We evaluate the effects of oxygen on accuracy by using air as the injectant. Toluene fluorescence is strongly quenched by oxygen and exhibits a fluorescence red shift due to oxygen for certain excitation wavelengths [18]. Negligible oxygen-induced red shift has been observed for 266-nm excitation [33]; however [18] proposed a model based on two de-excitation channels to describe the effect of oxygen number density on the decrease in (total integrated) FQY. Their model is used here.

The ratiometric thermometry scheme using toluene with 266-nm excitation can be used in environments with and without oxygen, and with or without mixing. This conclusion is valid only if oxygen quenching results in a decrease in FQY (spectral and integrated) without deforming (e.g., red shifting), the fluorescence spectrum over the range of (pressure/temperature) conditions of interest. Unfortunately, there is not sufficient information to unequivocally establish this conclusion. The only available but limited, amount of data supporting this conclusion is from the work of [18] and from some of their unpublished data [33]. Under this assumption, the role of oxygen is to quench fluorescence uniformly across the fluorescence spectrum. Thus, Eq. 2 is modified to introduce the effect of quenching on $\phi(\lambda, T)$ using the model of [18]. Then, the corresponding conversion curve $R(T)/R(T_{\text{ref}})$ versus T can be constructed similarly to the oxygen-free case. Because quenching is independent of wavelength, the resulting $R(T)$ calibration curve is identical to the one for the oxygen-free case. However, oxygen quenching strongly reduces fluorescence, thus negatively impacting the accuracy of the measurement or even hindering altogether its applicability in practice.

Although low FQY (thus LIF signals) is expected in flows with oxygen, it is expected that reasonably accurate measurements of temperature might also be achieved in flows with oxygen. [26] have shown that good temperature measurement in uniformly seeded, oxygen-free flows can be performed up to 700 K, and up to 900 K with a somewhat reduced accuracy and reasonable signal-to-noise ratio. Therefore, based on the model and restrictions considered here, it is expected that acceptable temperature measurements are also possible in flowfields with oxygen (e.g., air) or in non-uniform flows with mixing in the presence of air.

3 Experimental setup

In this study, we consider a transverse jet in supersonic crossflow generated by injecting a fluid perpendicularly to the flow over a flat plate generated by an expansion tube.

3.1 Supersonic flow facility

The experiments presented herein were conducted at the 6" Expansion Tube Facility of the High Temperature Gasdynamics Laboratory at Stanford University. This facility was used to generate the supersonic crossflow used to test the PLIF method in the transverse jet configuration described here. A detailed description of this facility can be found in [34] and [35]. A general treatment of the operational principle and theoretical analysis of the performance of an expansion tube can be found in [36].

The crossflow was generated using nitrogen seeded with toluene vapor (0.5 % by volume) as the test gas. To ensure uniform and repeatable seeding, the toluene/nitrogen mixture was prepared manometrically in a separate tank and then used as the test gas in the expansion tube. A low-enthalpy crossflow was considered to avoid toluene pyrolysis and ensure large fluorescence yields.

Throughout the study, the freestream conditions were maintained constant at a Mach number $M_a = 2.3 (\pm 0.1)$, pressure $p_a = 111 \text{ kPa} (\pm 10 \text{ kPa})$ and temperature $T_a \approx 460 \text{ K} (\pm 10 \text{ K})$, with a test time duration of approximately 2 ms (over which M_a was steady to within 10 %). Subscript a refers to freestream conditions. The aerothermal conditions of the crossflow reported here were estimated from an initial set of flow calibration runs and from a measure of the shock speeds acquired during the experiments and from which nominal, bulk-average conditions were inferred using a zero-dimensional expansion tube solver (based on the expansion tube analysis of [36]). The set of flow calibration runs consisted of measuring the freestream Mach number from Schlieren images, and measuring the pitot-static pressure acquired in the freestream. Shock speed measurements were acquired as the time-of-flight between pressure sensors mounted along the expansion tube at the driven and expansion sections. Further details on the quantification of the crossflow aerothermal properties are provided in [26].

3.2 The transverse jet in supersonic crossflow

To demonstrate the methodology, a transverse jet in supersonic crossflow system was considered and investigated. Referring to Fig. 1, the flow of interest was generated by issuing a jet of fluid perpendicularly from a flat plate into

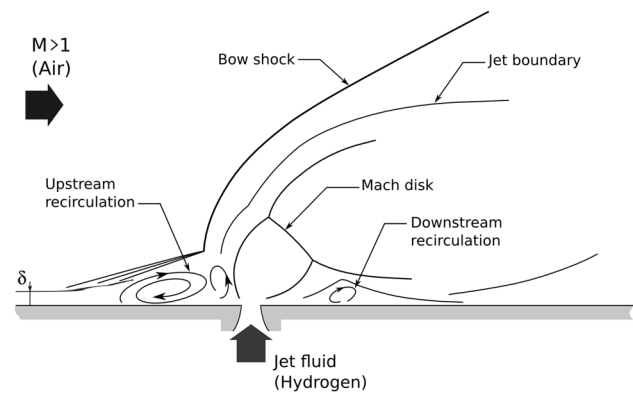


Fig. 1 Schematic diagram of the flowfield of a transverse jet in supersonic crossflow

the supersonic crossflow of nitrogen seeded with toluene. Injection was carried out from room temperature (i.e., the stagnation temperature of the jet was near 295 K) conditions at a suitable value of the jet stagnation pressure (around 1.9 MPa, depending upon the fluid being used). The flat plate (155 mm long by 100 mm wide) was placed at the exit of the expansion tube within the region of uniform flow. The jet fluid was injected from a contoured round orifice 2 mm in diameter (D) located 64 mm from the leading edge of the flat plate. Different injection gases were employed to assess PLIF thermometry measurements under different fluid conditions. In particular, injection of hydrogen, helium, helium/argon (85 %/15 %) mixture, nitrogen, air and argon were considered. Although none of these fluids affect the spectroscopy of toluene (other than air), they do affect the temperature field (through different specific heats) and the structure of the JISCF. These fluids were selected to investigate the physics of mixing for variable-density JISCFs, which will be reported in a separate publication. Within the scope of the current study, this range of fluids was considered to investigate the impact of fluid properties (primarily the specific heat of the fluid) on the use of toluene PLIF for thermometry and as a measure of mixing. In presenting the results in the following sections, we will solely consider the hydrogen and argon cases, having the extreme values of molecular weight and specific heat considered in the study. We will also consider the air injection case to assess how oxygen quenching affects our ability to accurately measure temperature in these flows.

The set of cases considered in the investigation are summarized in Table 1 where the main parameters defining the transverse jet are reported. In particular, the jet-to-crossflow density ratio (s), velocity ratio (r), and corresponding momentum flux ratio (J) are reported. The jet exit Reynolds number (Re_D) defined as $\rho U_{jet} D / \mu$ based on exit conditions

Table 1 Summary of jet conditions

Gas	s	r	J	Re_D
H ₂	1.65	1.21	2.4	3.3×10^5
He	3.07	0.89	2.4	2.1×10^5
85 % He/15 % Ar	7.17	0.58	2.4	3.1×10^5
N ₂	22.9	0.32	2.4	6.4×10^5
Air	23.7	0.32	2.4	6.0×10^5
Ar	30.6	0.28	2.4	5.8×10^5

s , r and J are the jet-to-crossflow density ratio, velocity ratio, and momentum flux ratio, respectively; Re_D is the jet exit Reynolds number based on exit conditions

is also reported. All cases were selected to maintain a constant value of $J = 2.4$.

3.3 Imaging configuration

The excitation and detection configuration used in the current study mostly followed the methodology and configuration used in [26]. The excitation laser light was provided by a frequency-quadrupled injection-seeded Nd:YAG laser. The resulting laser beam was directed to the test section where it was formed into a collimated 4-cm-wide laser sheet through a combination of cylindrical lenses and then focused to a (FWHM) thickness of about 0.4 mm (measured with the scanning knife edge technique).

Following 266 nm excitation, fluorescence was collected with two separate ICCD cameras equipped with suitable collection optics and filters. In particular, an Andor iStar 712 (512×512 pixel) and a LaVision DynaMight (2×2 binned to 512×512 pixel) ICCD cameras were used. The ICCD cameras were gated to 400 ns to capture all fluorescence while reducing collection of unwanted background light. Each camera viewed the imaging region from opposite sides of the laser sheet and was adjusted to match magnification and field-of-view. The resulting spatial resolution was $96 \mu\text{m}/\text{pixel}$, which is near the resolving power of the imaging arrangement.

In the dual-wavelength collection scheme used here, each camera collected a different spectral band of toluene fluorescence by imaging through different optical filters. In particular, the DynaMight ICCD camera was equipped with two interference bandpass filters centered at 280 nm with ± 10 nm FWHM bandwidth (BP280) and one UG11 Schott glass filter; conversely, the iStar ICCD camera used a 3-mm-thick WG 305 long-pass filter and UG11 filters. To facilitate the discussion, with reference to the filters used for the imaging, we will here refer to each individual view as the “BP280” (or “blue”) and “WG305” (or “red”) views, respectively.

3.4 Image correction and processing

In this section, we summarize the image correction and processing steps that were used to extract the final temperature fields. Because the method is based on a ratiometric approach from two independent camera views, it is imperative that the imaging from each view is accurately matched (to sub-pixel accuracy) to prevent errors in the temperature measurement arising from registration mismatch and to preserve the features of complex turbulent flows with good fidelity. To anticipate a result shown below, it was found that residual registration errors of even sub-pixel magnitude resulted in significant fictitious gradients in the reconstructed temperature field associated with turbulent features. This effect was particularly evident near sharp discontinuities, such as at the bow shock of the JISCF. Therefore, to enhance the image registration accuracy, a multi-step image registration, dewarping and correction scheme was employed following background subtraction (from an ensemble average background image). In particular, the image correction procedure was structured in the following three steps.

Step 1 Initial camera registration was carried out by imaging a target composed of a matrix of equally spaced dots marked on a transparent film and located at the center of the excitation laser sheet. From this target image, the initial registration projection function needed to project one view (red) onto the other one (blue, which we take here to be the reference view) was constructed. This initial registration step achieved projection errors less than 0.1 pixel (projection error was defined as the difference between the centroid of dot markings extracted from the reference view and of that from the projected second view).

Step 2 The second step was to correct for accidental misalignment (primarily translation) between the two views on a shot-to-shot basis. This step was found necessary to account for residual translation (mainly lateral) arising during operation of the facility over the course of the day. For this purpose, registration features were introduced at the edges of the illumination laser sheet by modulating its intensity with thin wires [37], from which the relative lateral offset between the two views was extracted and used to compensate the pair of images on a shot-to-shot basis.

Step 3 As last step, any further post-processing required to reduce the data was carried out (e.g., background subtraction and sheet correction), the two shot-to-shot matched views ratioed and the corresponding temperature field reconstructed using the calibration curve constructed in Sect. 2. Only as the final step, the resulting images were dewarped to project them from the image coordinate system to the object coordinate system. This last step also corrected any image deformation introduced by the imaging system.

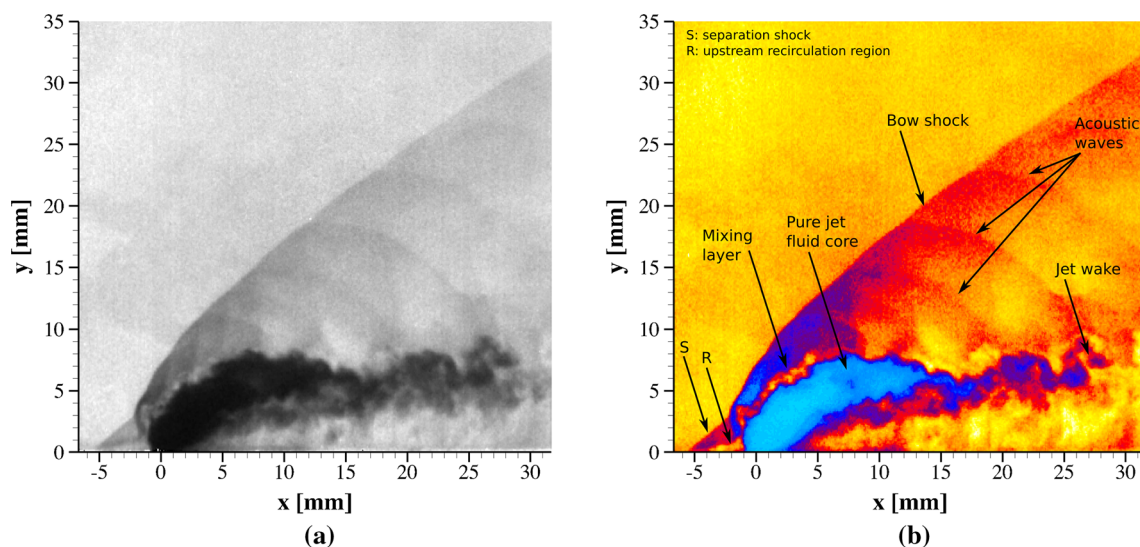


Fig. 2 PLIF image of the transverse jet: **a** WG305 view (*grayscale colormap*), and **b** BP280 view (*colormap from blue to red to yellow*) for hydrogen injection. In all cases shown here, $J = 2.4$ and the freestream Mach number and temperature are 2.3 and 460 K, respectively

Note that this set of dewarping, matching and image resampling steps have to be kept in mind when interpreting the signal-to-noise ratio (SNR) values obtained in the current study. In fact, each step effectively acts as a low-pass-filtering operation, thus improving the SNR value.

4 Imaging results

4.1 Imaging in an oxygen-free environment

An example of the LIF images acquired simultaneously with the red and blue cameras are shown in Fig. 2a, b, respectively, after all image correction steps were taken. The case shown in this figure refers to hydrogen injection. Because each view is sensitive to a different portion of the fluorescence spectrum, the same features are rendered in a slightly different way and hence can be an aid for the interpretation of the overall structure of the JISCF flowfield.

The results of these introductory images show that the strong temperature sensitivity of toluene fluorescence is capable of capturing and effectively rendering all the major flow structures (refer back to Fig. 1 and to the labeled features of Fig. 2b): the bow shock, the (upstream) separation shock (S), and the edge and wake of the transverse jet. Note also that jet fluid entrainment in the upstream separation region is well-captured as the high LIF signal region near the wall upstream of the injector reveals (R).

The exceptional temperature sensitivity of the toluene LIF is also demonstrated by what we identify in Fig. 2b as acoustic waves. They are seen to radiate outward from the

transverse jet origin into the region bounded upstream by the corrugated bow shock and below by the wake of the jet.

These images also reveal the near-field, windward mixing layer generated by the penetrating jet (unseeded) and the crossflow (toluene seeded). This fluid dynamic feature is well-rendered by the high-intensity LIF signal band that can be recognized past the quasi-normal portion of the bow shock (where there is low LIF signal due to high temperature past the shock) and the core of the jet (where there is no LIF signal due to lack of tracer). The mixing layer is rendered as shown here because of the non-uniqueness of the LIF signal on the local fluid state. A similar effect could be expected with other tracers, but toluene exhibits this property very strongly because of the exponential temperature sensitivity while only a linear dependence on tracer mole fraction.

Figure 3a shows an example of the LIF ratio. Then, by applying the LIF ratio to temperature calibration, the ratio is converted to temperature as shown in the final result of Fig. 3b. The blanked out portion (shown in white) of the flowfield in Fig. 3b is the portion of the jet where pure jet fluid exists and where temperature measurements cannot be performed; it has been defined based on a threshold value of the LIF signal set to 5 % of the free stream value.

The image of the fluorescence ratio and reconstructed temperature generally result in a flowfield with less fine-scale details than what the PLIF images might suggest, while maintaining the underlying structure of the system being investigated. Loss of detail is only apparent in the sense that many of the features that can be identified in the PLIF image result from the large spatial contrast

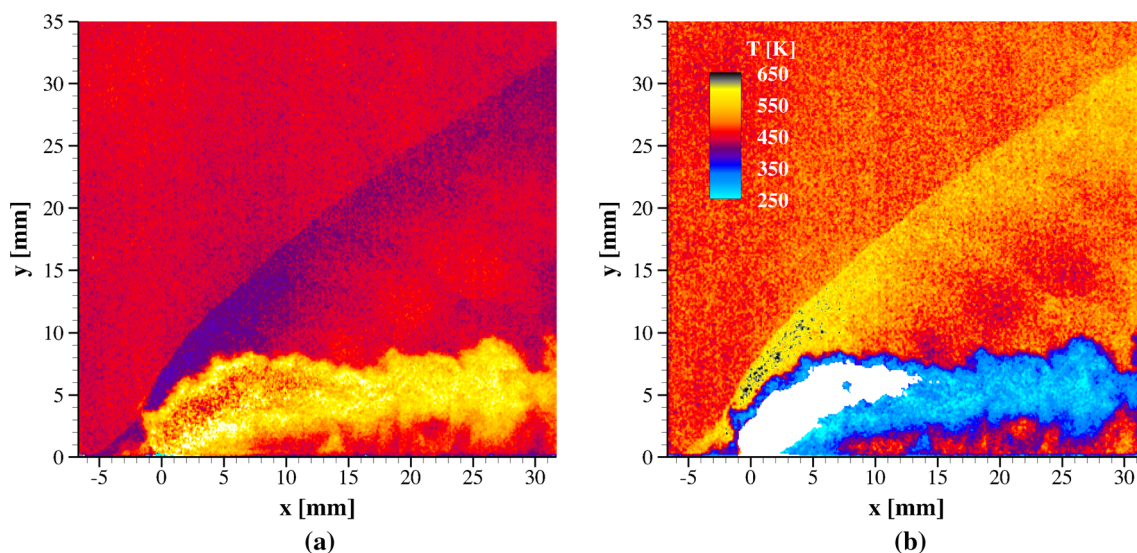


Fig. 3 **a** LIF signal ratio BP280/WG305 and **b** reconstructed temperature field corresponding to the case of Fig. 2

enabled by the high temperature sensitivity of the fluorescence. Referring again to the labeled features of Fig. 2b, the temperature rise across the bow shock and across the separation shock are clearly captured; very clear also is the presence of colder fluid in the upstream separation region (an important feature in JISCF). The acoustic waves identified in the LIF images of Fig. 2b can also be recognized in Fig. 3b.

The measured temperature and one of the LIF image were combined with Eq. 1 to infer the number density (n) of the tracer (in freestream fluid) to be used as a more fundamental measure of mixing. In order to account for shot-to-shot variation of crossflow properties, the number density was normalized by the freestream value, n_a . The normalized number density n/n_a was further reduced to a measure of the partial pressure of the tracer by removing the temperature effect on n , thus reducing to $\chi p/\chi_a p_a$, where χ and χ_a are the local and freestream values of the mole fraction of tracer, respectively.

To give an example of typical measurements, Figs. 4 and 5 show an example of the measured instantaneous LIF signal, temperature, normalized number density n/n_a and normalized partial pressure $\chi p/\chi_a p_a$ for injection of hydrogen and argon, respectively. Because no low-pass-filtering operation was performed at any step in the data reduction process, measurement noise has been amplified. This can be qualitatively assessed by looking at the gradual worsening of the SNR of each field. Qualitatively, the LIF images look acceptable, the temperature field appears noisier, and the partial pressure measurement is significantly noisy, thus preventing accurate local measurement. Nevertheless, the main features of the system can still be qualitatively

identified. A comprehensive assessment of the noise characteristics of these measurement will be provided below.

4.2 Imaging in flows with oxygen quenching

The feasibility of using toluene PLIF for temperature imaging in supersonic flows in the presence of oxygen was also investigated by considering the JISCF formed by injection of air into the toluene-seeded nitrogen crossflow.

Figure 6 shows an example of the (a) LIF signal (blue image) and (b) corresponding reconstructed instantaneous temperature for one case with air injection. Comparison of the LIF image obtained in this case with any of the previous cases (in particular with the argon case) reveals the impact of the strong oxygen quenching of the fluorescence as the jet fluid entrains and mixes with the hot crossflow. The strong oxygen quenching affects how the entire JISCF flowfield is visualized. In particular, the interface between the jet and crossflow is clearly rendered and identifies the interface where turbulent mixing occurs. On the jet side, the LIF is strongly reduced and helps identify regions where molecular mixing has occurred. Thus, in general, the strong quenching can be exploited to better identify regions of entrainment. For example with reference to Fig. 6a, oxygen quenching enables visualization of jet fluid entrainment into the upstream separation region or into the boundary layer downstream of the injector. These features are not as clearly rendered by the LIF signal when quenching is absent (e.g., Fig. 5a). Thus, the combination of both cases with and without oxygen quenching can be used in tandem to better explore the subtleties of the mixing process in these complex supersonic flows.

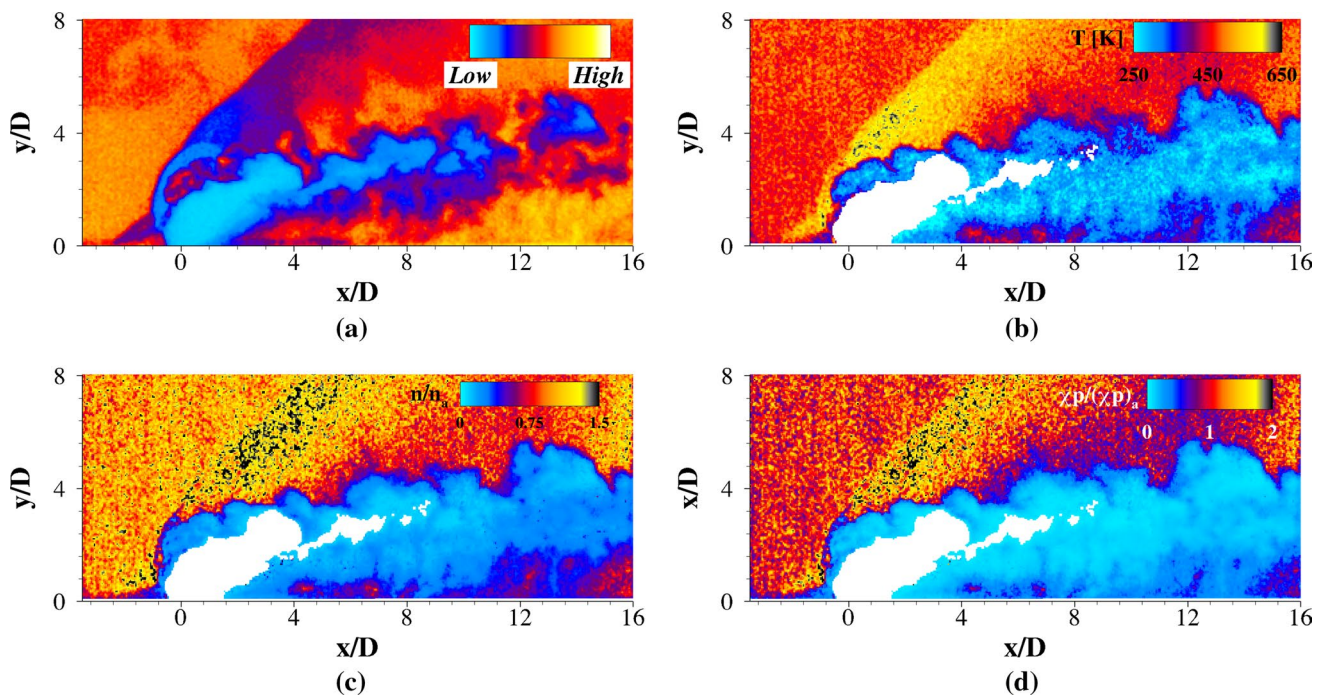


Fig. 4 Instantaneous fields for hydrogen injection: **a** BP280 LIF, **b** temperature, **c** number density and **d** partial pressure

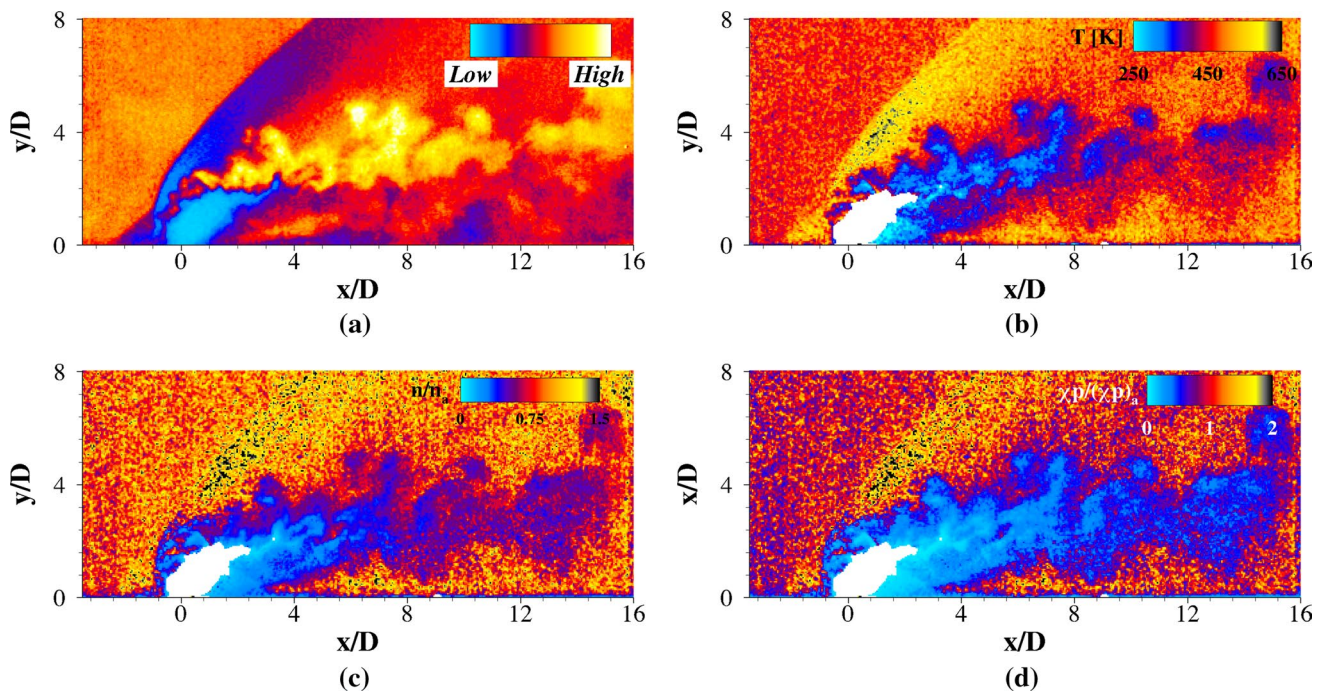


Fig. 5 Instantaneous fields for argon injection: **a** BP280 LIF, **b** temperature, **c** number density and **d** partial pressure

The corresponding reconstructed temperature field is shown in Fig. 6b. The first observation is that the resulting temperature field is noisier and more fragmented (compared to an equivalent case with no oxygen quenching).

For example, in the previous case of Fig. 5, the large-scale structures were better rendered and could be more easily identified by inspection. On the contrary for the air case, the regions associated with the transverse jet (the cold

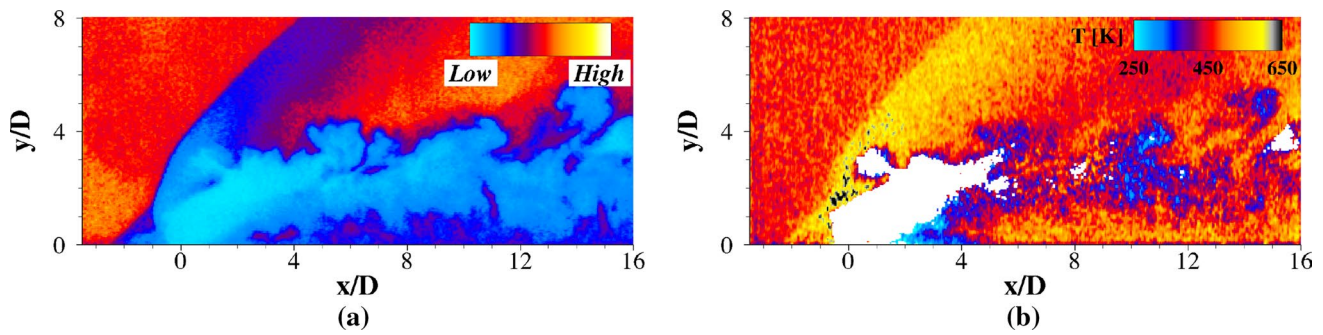


Fig. 6 Instantaneous fields for air injection: **a** BP280 LIF, and **b** temperature

regions) are not smooth and are noisy and difficult to discern. From a comparison of the set of data available, we believe that the result of Fig. 6b are solely due to the low SNR and low signal levels that exists (within the wake) in the case where oxygen quenching is present.

Unlike the oxygen-free case, in this case, extracting the number density field directly from the LIF measurements is not possible. When oxygen quenching is present, the relationship between LIF and local number density depends on both pressure and χ (knowing temperature). But because the LIF signals from the two channels are not independent, it is thus not possible to infer either of them, not even in a relative form as done for the quenching-free case.

5 Temperature measurement accuracy

In this section, we evaluate the accuracy of toluene PLIF thermometry applied to non-uniform mixing flows. A more complete assessment is carried out based only on the oxygen-free case, whereas the analysis for the case of air injection (i.e., with oxygen quenching) will be of more limited scope. First, we will investigate the response of the methodology to different working parameters related to the transverse jet in crossflow system; then, we will assess the accuracy of the measurements by comparing to expected values, based on SNR consideration and including errors associated with image registration, which was found to have a large contribution and it is of particular importance in our application.

5.1 Measurement response analysis

A simple, zero-dimensional model of the mixing process in non-uniform flows was constructed to investigate the response of the toluene PLIF thermometry (without and with oxygen quenching) to different working parameters relevant to this study. The main working parameter was the type of fluid employed for the injection. For each injectant,

two properties are of particular interest: molecular weight (W) and specific heat (c_p). They both affect the resulting mixing and how the resulting LIF signal is rendered, but they do not affect the spectroscopy of toluene itself. Injection of different fluids might also affect the fluid dynamics of the JISCF system [38, 39]. We will first focus on the oxygen-free case, and later extend the analysis to the case with oxygen.

5.1.1 Oxygen-free case

The zero-dimensional model considers the mixing of a given amount of crossflow fluid (nitrogen) with a given amount of jet fluid (as in Table 1). We define ζ the mass fraction of jet fluid in the mixture (i.e., we interpret it as the mixture fraction). We assume that each fluid is at an initial temperature T_a (freestream) and T_j (jet), respectively. As an example, we consider $T_a = 650$ K (which is near the maximum temperature seen in these experiments in the post-bow shock region) and $T_j = 295$ K (which is the temperature of the injectant). From an energy balance, the temperature of the resulting mixture is thus:

$$T(\zeta) = \frac{\zeta c_{p,j} T_j + (1 - \zeta) c_{p,a} T_a}{\zeta c_{p,j} + (1 - \zeta) c_{p,a}} \quad (3)$$

Furthermore, assuming an initial value of pressure (taken to be 100 kPa in the model), the corresponding number density can also be constructed as a function of mixture fraction. Pressure was assumed to remain constant during the mixing process. Then, given a mixture (i.e., the type of jet fluid and the value of ζ) and its corresponding temperature, the corresponding full-spectrum, BP280 and WG305 LIF signals and the (BP280/WG305) LIF ratio were constructed using the model described in Sect. 2.1. In doing this, it was assumed that toluene was seeded into the freestream nitrogen with an amount of 0.5 % by weight (as in the experiments themselves).

Figure 7 shows plots of the (a) mixture temperature, (b) BP280 LIF signal and (c) LIF signal ratio as a function of

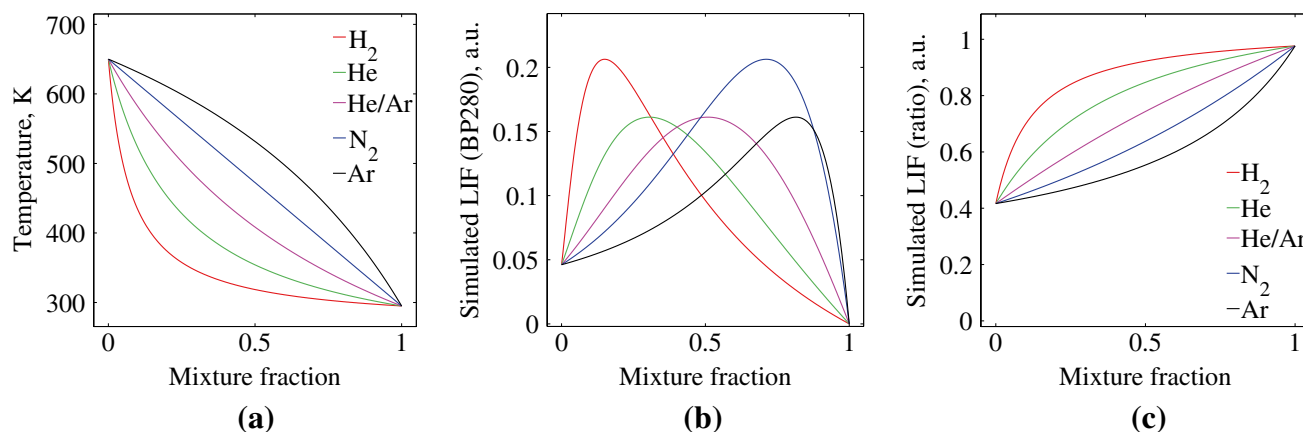


Fig. 7 **a** Temperature of the mixture as a function of mixture fraction; **b** corresponding simulated BP280 LIF signal and **c** (BP280/WG305) LIF ratio for different room temperature jet fluids mixing with hot (650 K) nitrogen

mixture fraction for the different jet fluids considered in this study ($\zeta = 1$ indicates pure, unseeded jet fluid). The temperature profile (Fig. 7a) shows the trivial nonlinear (but still monotonic) relation between the two quantities due to the different properties (c_p) between fluids. Most interestingly, it is the LIF signal profile (Fig. 7b). For all fluid cases, the profile is non-monotonic with a maximum LIF signal for an intermediate value of ζ that depends on the combination of working fluids. In particular, for heavy gases like N_2 and Ar, the peak LIF signal approaches $\zeta = 1$ while for light gases like H_2 and He, it approaches $\zeta = 0$. The WG305 and full-spectrum LIF signals show a similar behavior. This non-monotonic behavior of the LIF signal is solely due to the strong temperature sensitivity offered by toluene PLIF even though the dilution of tracer and the temperature are monotonic in ζ . In particular, as Fig. 7a shows, our choice of the configuration of the diagnostic is such that both the mixture temperature and the number density of the tracer molecule (toluene) decrease as ζ increases (because we are seeding the hot freestream and not the jet). Referring back to the LIF equation (see Eq. 1), the LIF signal depends on the product of the number density of the tracer (a monotonic decreasing function of ζ) and the FQY, which has an exponential dependence on temperature (neglecting for sake of discussion the relatively weak temperature dependence of the absorption cross section of toluene for 266-nm excitation). Thus, the FQY strongly increases as temperature decreases due to the mixing (as ζ increases). The result is a strong LIF signal increase as mixing occurs (as ζ increases). Then, due to the dilution of the tracer species, as we approach $\zeta = 1$, the amount of tracer in the mixture goes to zero and the LIF signal is forced back to zero. The competition between these effects results in the non-monotonic behavior observed in Fig. 7b. Finally, both the BP280 and WG305 LIF signals

are affected in a similar fashion, thus their ratio becomes again a monotonic function (albeit not linear) of ζ . This is demonstrated in Fig. 7c. It is also interesting to note that the relationship between the LIF ratio and ζ is generally not linear and the exact dependence between the two quantities is affected by the properties of the mixing species. Note, however, that a nearly linear dependence can be obtained for a particular jet fluid (in this case the Ar/He jet mixture mixing with nitrogen).

Figure 8 shows the same results of Fig. 7 but cast in terms of temperature dependence. In this form, the only relevant parameter that differentiates the behavior is the ratio of specific heats γ . The results presented in this form show the non-monotonic relationship between the LIF signal and the fluid properties. The non-monotonic behavior remains in both temperature and (freestream normalized) number density dependence, while a nearly linear dependence between LIF ratio and (normalized) number density is observed.

In our flow, compressibility changes both temperature and pressure. However, it will not alter the overall monotonic dependence on ζ , nor it will affect the strong temperature sensitivity of the toluene LIF. Therefore, it is expected that the same qualitative behavior exists once compressibility effects are in place.

5.1.2 Oxygen quenching case

The same model (and with the same initial temperature and pressure) was also extended to the case where oxygen quenching is present. This case replicates conditions where experiments were conducted in the same nitrogen freestream (as the other experiments) but injecting air as the jet fluid. This model is constructed similarly to the previous case with nitrogen and suffers from the same limitations.

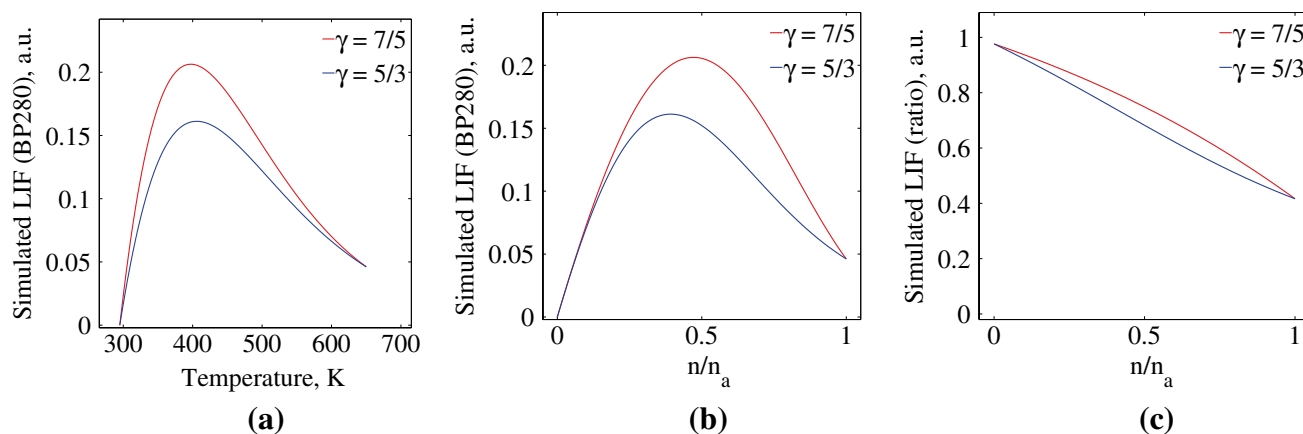
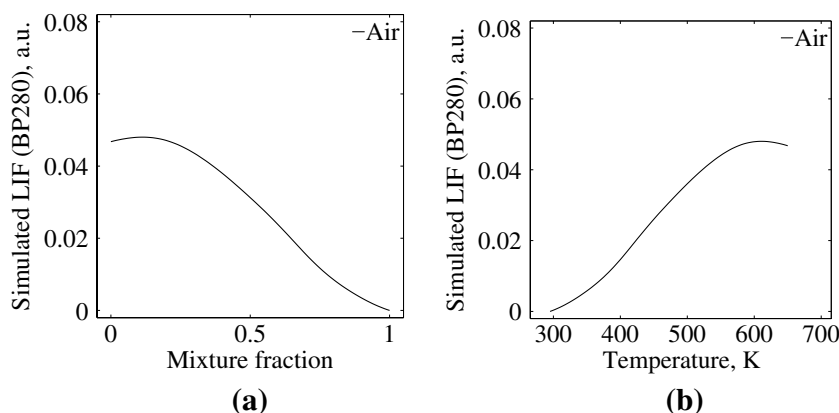


Fig. 8 **a** Simulated BP280 LIF as a function of temperature of the mixture for jet fluids with $\gamma = 5/3$ and $\gamma = 7/5$; **b** corresponding simulated BP280 LIF signal and **c** (BP280/WG305) LIF ratio as a function of normalized number density

Fig. 9 **a** Simulated BP280 LIF signal as a function of mixture fraction; and **b** simulated BP280 LIF signal as a function of temperature for mixing with oxygen quenching



The only difference is that the LIF model accounts for oxygen quenching as described in Sect. 2.2, and it assumes that air is composed of 21 % oxygen in nitrogen. The results of the model for this case with oxygen quenching are shown in Fig. 9.

In this case, the relationship between temperature of the mixture and ζ (not shown) is identical to the nitrogen injection case of Fig. 7a. However, when oxygen quenching is present, the dependence of the LIF signal (e.g. the BP280 LIF signal) with ζ (Fig. 9a), or with temperature of the mixture (Fig. 9b) is altered from the oxygen-free case (compared to the nitrogen injection cases of Figs. 7 and 8). In particular, the non-monotonic behavior is strongly reduced and it weakly appears near $\zeta = 0.15$. Although it is not shown here, the exact profiles of Fig. 9 depend on the oxygen content and on the initial conditions. The important aspect to highlight here is that the presence of oxygen reduces or completely removes the non-monotonic behavior, thus hindering some of the benefits of toluene PLIF imaging. As it was noted in Sect. 2.2 based on the model presented there, the LIF signal ratio is insensitive to the

presence of oxygen quenching, thus the same dependence between LIF ratio and ζ is found in this case.

5.2 Potential localized pressure dependence and accuracy

One of the limitations of toluene PLIF is that pressure dependence on FQY might exist for low pressures [20, 28]. The nominal conditions of the experiments performed here were selected to be in the pressure-independent regime, at least in a bulk sense. However, the flowfield generated by a JISCF is complex and highly non-uniform in pressure, temperature and (jet fluid) concentration. The crossflow static pressure was maintained above 100 kPa, and the local static pressure increases as the bow shock system is encountered. However, wall static pressure measurements in JISCFs have indicated that the leeward region of the transverse jet experiences static pressures well below the freestream static value [40, 41]. In particular, pressure sensitive paint measurements show that there is a strong compression in the windward side that may amount to several times the

freestream values (depending upon the value of J); the compression is due to the upstream separation and the bow shock. On the contrary, the flow experiences a sudden expansion at the leeward side, with pressures that can be as low as one quarter of the freestream value. This low-pressure region resides in a limited portion of the wake of the transverse jet and extends downstream up to about $5D$ (for transverse jets with J similar to these experiments). Thus, for the case of this study, the value of the minimum pressure that the flow experiences in the low-pressure region is estimated to be as low as 25 kPa. This value is well within the pressure-dependent regime [20].

Pressure dependence may affect the results by altering the dependence of the LIF ratio with temperature through the following two mechanisms: (1) a change in the magnitude of the integrated FQY, and/or (2) a distortion of the spectral FQY. For 266-nm excitation, the integrated FQY remains constant from total pressures larger than 80 kPa. Below this value, the limited data of Cheung [20] (taken at room temperature) suggests that the integrated FQY increases at most by about 20 % as pressure is lowered. A limited set of spectral FQY data is also available from Cheung [20] at different pressures (at room temperature). For total pressure above 100 kPa, there is no measurable change in the spectral FQY with increasing pressure (at room temperature). Low-pressure spectral FQY was measured for pure toluene at 10 and 20 mbar and indicate a small, but measurable, decrease of the spectral FQY for wavelengths below about 270 nm; for larger wavelengths, the spectral FQY remains unaltered.

Although a comprehensive assessment cannot be drawn because of the limited data available, what known suggests that pressure effects might be negligible here. Pressure-induced changes that do not alter the spectral distribution of the FQY do not affect the LIF ratio to temperature mapping function. Furthermore, because of the use of the BP280/WG305 optical filter combination, the portion of the spectral FQY that may depend on pressure is removed from the integral of Eq. 1 for both the blue and red views.

It is thus concluded that the inferred temperature is robust relative to large changes in local pressure for the detection arrangement used in this study irrespective of the flow conditions. On the contrary, measurement of the number density in low-pressure environments (below 80 kPa) do have a dependence on pressure through changes in integrated FQY. Quantification of the exact impact or even accounting for this component is currently not possible due to lack of information in this regard. Nevertheless, because the inferred number density depends linearly on the integrated FQY, it is expected that the error in number density could be at worst 20 % for pressure reaching below 10 kPa.

5.3 Precision evaluation (SNR)

Measurement precision is here defined and evaluated in terms of the spatial signal-to-noise ratio (SNR). The SNR was defined by extracting sub-regions of size $N \times N$ from the images from which the mean (\bar{S}) and standard deviation (σ_S) values over the subregion were computed. Then SNR was defined as the ratio \bar{S}/σ_S , where S is any quantity of interest, like the LIF signal, temperature, number density, etc. Values of $N = 4, 8$ and 16 were considered. Note, however, that this method does not differentiate between spatial variations inherent with the spatial variability of the flow and true measurement noise. Probability density functions (PDF) of the SNR for the different quantities were then compiled and are shown in Fig. 10. The effect of increasing N was to remove the tails at high SNR in the distributions of Fig. 10.

The results for the LIF signal indicate SNR values near 45–50 in the freestream where the highest temperature (lowest LIF values) is found, and SNR values near 15 in the wake of the transverse jet where temperature is low but less tracer is present. However, because of turbulent mixing in the wake, true spatial variations in the flow may also contribute to a lower estimate of the SNR. For the temperature field, SNR on the order of 25–30 can be achieved, even

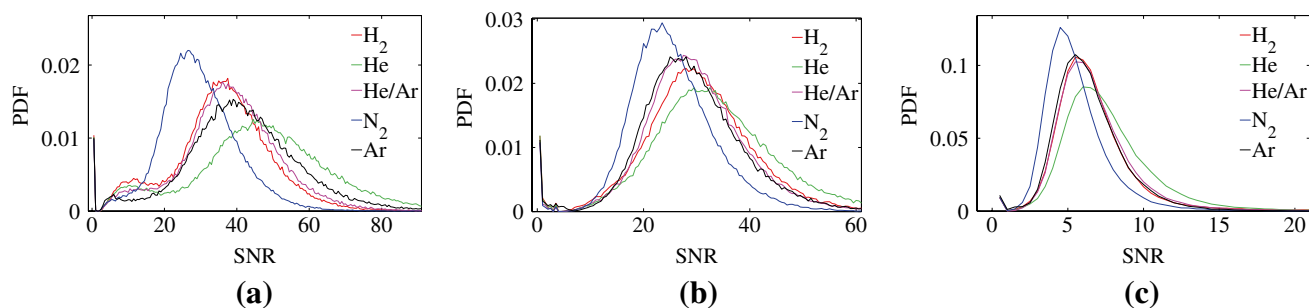


Fig. 10 PDF of local spatial SNR computed for the **a** corrected WG305 LIF image, **b** temperature and **c** partial pressure. SNR is computed over a 4×4 pixels

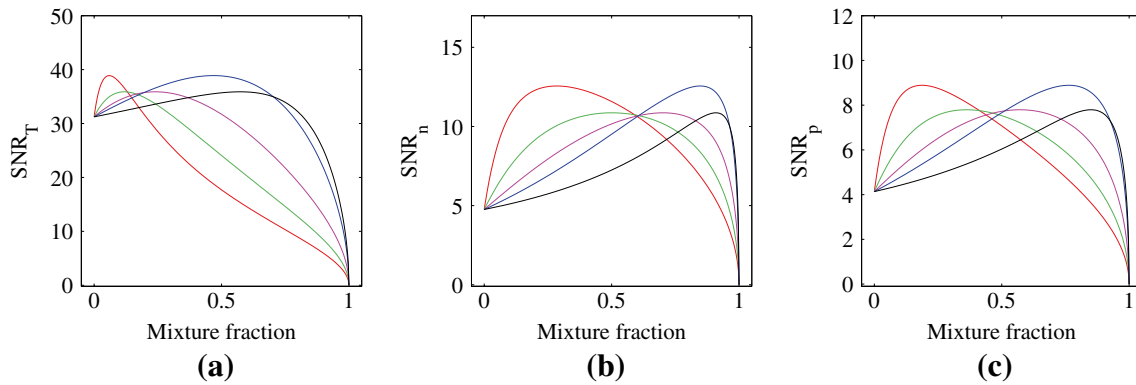


Fig. 11 Expected variation of SNR for **a** temperature, **b** number density, and **c** partial pressure with mixture fraction for different room temperature jet fluids mixing with hot (650 K) nitrogen. Legend scheme as Fig. 7

in the wake of the jet. Finally, for the number density and partial pressure, the SNR is only around 5. Thus, the estimation of the number density results in a decrease in the SNR by a factor of 5 from that of the measured LIF and temperature fields.

For comparison and for investigating the expected variation of SNR with mixture fraction, the expected SNR for all quantities of interest can also be estimated using the LIF and mixing models outlined previously. In particular, the SNR of the temperature measurements can be estimated from the calibration function above and the SNR values of the two LIF channels as [26]:

$$\frac{1}{SNR_T} = \frac{R}{T} \frac{dT}{dR} \sqrt{\frac{1}{SNR_{f,1}^2} + \frac{1}{SNR_{f,2}^2}} \tag{4}$$

where $R = S_{f,1}/S_{f,2}$ as defined previously, and $SNR_{f,1}$ and $SNR_{f,2}$ are the SNR values of the two LIF channels. The term dT/dR can be estimated from the ratiometric calibration above. The only unknowns in the equation are $SNR_{f,1}$ and $SNR_{f,2}$, but for simplicity we here estimate them assuming that the LIF is shot-noise limited, i.e., $SNR_{f,i} = \sqrt{S_{f,i}}$. Furthermore, using the error propagation equation, the corresponding SNR for the number density as a function of the SNR of the LIF signal and of the measured temperature can also be derived and written as:

$$\frac{1}{SNR_n^2} = \frac{1}{SNR_f^2} + \left[\frac{T}{\sigma(T)} \frac{\partial \sigma}{\partial T} + \frac{T}{F(T; \Omega_\tau)} \frac{\partial F(T; \Omega_\tau)}{\partial T} \right]^2 \frac{1}{SNR_T^2} \tag{5}$$

where for brevity $F(T; \Omega_\tau)$ is used to indicate the integral of Eq. 1 and SNR_f is the SNR of one of the two LIF channels used to estimate the number density. Similarly, the SNR for the partial pressure is a mere extension of SNR_n to give:

$$\frac{1}{SNR_p^2} = \frac{1}{SNR_f^2} + \left[1 - \frac{T}{\sigma(T)} \frac{\partial \sigma}{\partial T} - \frac{T}{F(T; \Omega_\tau)} \frac{\partial F(T; \Omega_\tau)}{\partial T} \right]^2 \frac{1}{SNR_R^2} \tag{6}$$

Using Eqs. 4–6 to estimate the variation of SNR for the three quantities with mixture fraction, Fig. 11 shows the resulting profiles for mixing of different room temperature jet fluids with hot (650 K) nitrogen. In constructing Fig. 11, the only free parameters were $SNR_{f,i}$ taken in the shot-noise limit and were scaled to give an SNR_T around 30, as seen in the experiments.

First, it is noted that imposing an appropriate value for SNR_T , the same magnitudes of SNR_n and SNR_p of what was observed in the experiments are recovered by Eqs. 4–6. For all three quantities and all fluid cases, it is observed that the SNR trend is again non-unique, as was observed for other quantities above. In fact, the overall trend of the SNR for all quantities primarily follows the trend of the LIF signal, as shown in Fig. 7b. In particular, the peak of the SNR is found for some intermediate values of the mixture fraction, and the peak depends on the type on injectant. For light gases, the peak is near $\zeta = 0$ and it moves toward $\zeta = 1$ for heavier gases. As far as temperature is concerned (Fig. 11a), light gases show a rapid decrease of SNR_T as ζ increases; on the contrary, for heavier gases, SNR_T tends to level out over a large range of the mixture fraction.

5.4 Temperature reconstruction errors due to image registration errors

One of the limitations of the measurements presented here is associated with image registration errors. During the data reduction process, it was observed that minute shifts (sub-pixel) between the blue and red views resulted in different

reconstructed fields. In particular, it was observed that the magnitude of the local temperature had a somewhat weak dependence on image registration, but the spatial distribution of temperature was considerably affected to the point that the structure of the underlying turbulent flowfield was distorted. Similarly, the local temperature gradients were strongly affected. The dominant error was found to be due to a residual relative offset between the blue and red views after all correction and registration steps were taken. This residual offset appeared to be associated with shot-to-shot motion of the imaging equipment. The combined expedients introduced to account on a shot-to-shot basis for any relative displacement of the imaging equipment were capable of limiting this residual offset. However, subpixel offsets still remained and were limited by detection of the registration marks and image resampling. Because the method is based on the ratio between two PLIF images, it requires that the two views overlap with good precision and identical spatial discretization (i.e., each pixel should overlap in space). In this section, we will explore how good the overlap needs to be to reconstruct the temperature field with acceptable fidelity and compare it with the accuracy of the image registration process that could be expected in practice. This aspect was investigated from two perspectives: first, the characteristics of the temperature field obtained from the measurements assuming that an offset between each view existed were quantified; then, the same analysis was carried out for synthetic PLIF images constructed from the temperature fields of LES computations of a transverse jet in supersonic crossflow under similar conditions. Since in this latter case we do know the true solution, a more complete analysis can be carried out to investigate this aspect.

Figure 12 shows a set of three temperature fields for the hydrogen injection case constructed from the same initial blue and red PLIF images, but assuming that the two views had a different amount of longitudinal (i.e., streamwise) shift. Only longitudinal shift was considered, primarily because this is the direction along which registration errors were most common in our experiments. However, similar findings should be expected if offset along other directions is considered. In practice, these temperature fields were constructed starting from the spatially matched blue and red views pair (i.e., after the dewarping and matching procedure) by shifting one of the two views (the red view) by a known amount (0.1, 1 and 2 pixels for the images of Fig. 12, respectively), ratiating them and then, reconstructing the temperature field. The resulting field was then compared to the field obtained with no relative offset (assumed to be the most accurate representation of the field), which is here referred to as the baseline field. Figure 12a shows the results from imposing a pixels offset between views of 0.1 pixel; this value approaches the accuracy of the image

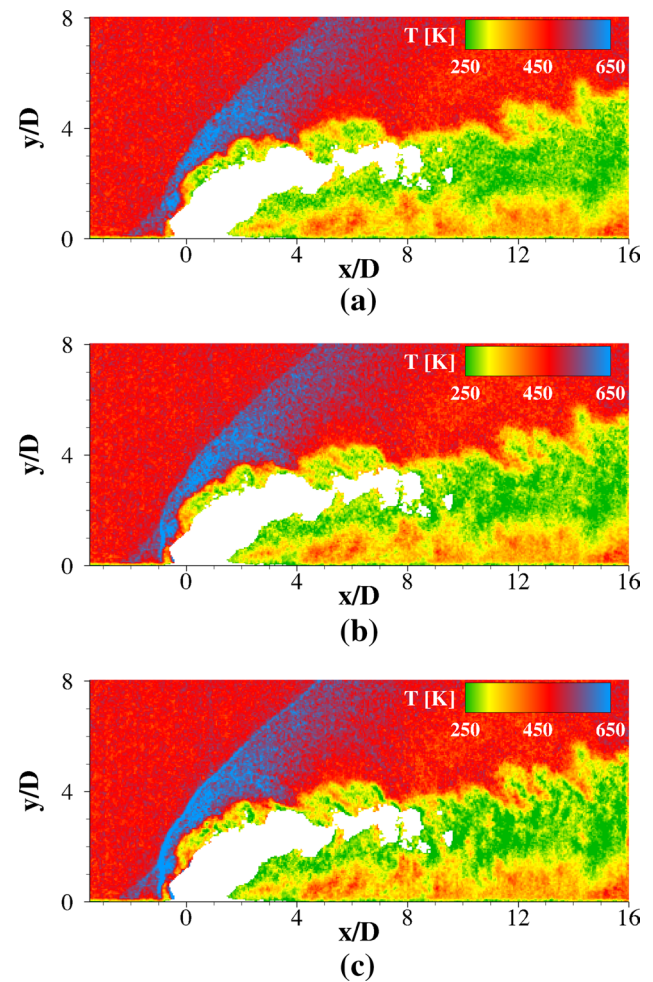
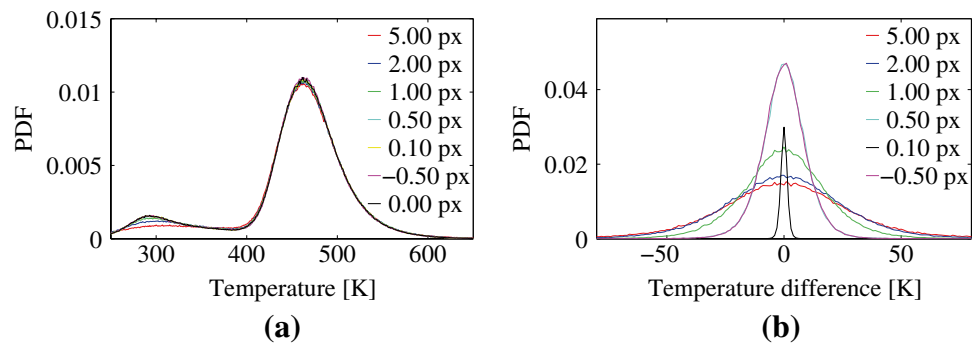


Fig. 12 Temperature field reconstructed after shifting the BF280 LIF image relative to the WG305 one of a known quantity: **a** 0.1 pixel, **b** 1 pixel, and **c** 2 pixels

registration procedure and the resulting field is nearly identical (it cannot be differentiated by visual inspection) to the original field. On the other hand, Fig. 12c considers an offset of 2 pixels, which is relatively a large amount and that results in artifacts that can be identified by direct visual inspection.

Comparing the three different cases with increasing amount of offset, it can be observed that, as the offset between the two views increases: (1) the (undisturbed) freestream temperature remains unchanged, (2) the temperature immediately past the bow shock increases; (3) the lower temperatures in the wake of the jet decrease; and (4) the spatial structures of the flow identified from the temperature field become sharper (i.e., the contrast increases). This last aspect is probably the most apparent effect, and the most troublesome, too. For example, by comparing Fig. 12a, c, it can be noted that the shock waves becomes sharper and that the contrast between the cold/hot edge

Fig. 13 **a** PDF of local temperature reconstructed after shifting the BP280 LIF image relative to the WG305 image of a known amount (indicated in legend). **b** PDF of the corresponding temperature difference



of the turbulent wake of the jet increases. In fact, Fig. 12c shows an increase in small-scale, low-temperature regions dwelling at the edge of the wake over what was observed for the low offset case (Fig. 12a) and the baseline field. An implication of this observation is that the spatial gradients of temperature could be greatly overestimated.

Figure 13a shows a PDF of the measured temperature computed assuming different amounts of longitudinal offsets. The PDFs were computed from all points in the measurement plane from different repetitions of the experiment. Although differences in the spatial distribution of temperature are observed from Fig. 12, the PDFs of Fig. 13a show nearly identical distributions other than some differences in the low-temperature portion. In particular, for small to moderate longitudinal offsets (less than about 1 pixel), the changes in PDF remain quite negligible. However, for offsets larger than 1 pixel, the low-temperature portion of the PDF flattens out (this portion is associated with the wake of the transverse jet). Thus, large errors in the measurement of the temperature of the wake can be expected. On the contrary, measurements in regions with large temperatures appear to be more accurate. This behavior is possibly the result of the fact that regions of large temperature are mostly spatially uniform (the most probable value in the PDF of Fig. 13a is the freestream value), thus an offset between the two views does not affect the temperature reconstruction process. On the other hand, low-temperature regions are associated with the turbulent wake of the jet, which is characterized by small-scale spatial variation of the temperature field. Thus, even minute offsets between the red and blue views can have a significant impact on the reconstructed temperature because the process uses values from regions with significantly different properties. Note that the different sensitivity to offset on the low and high temperature sides of the measurement is not a general result, but it applies only to the specific case of this study and it is linked to the spatial variation of the temperature field in this specific flow.

Figure 13b shows the PDF of the temperature differences between fields reconstructed imposing different amount of offsets and the baseline field. In general, the PDFs of the

temperature difference have a Gaussian-like shape with a width that increases with the amount of offset. For moderate pixel offset up to about 0.5 pixel, the temperature difference remains limited to values of order ± 20 K (which corresponds to about 4 % of the freestream value, or about 7 % of the stagnation temperature of the jet). As the offset increases over the 1 pixel limit, temperature differences can exceed ± 50 K, which is a significant fraction of the range of characteristic temperatures of this flow. Finally, note that as the offset increases, the curve of the PDF seems to reach a limiting profile, even though the actual spatial distribution of temperature is greatly distorted.

The results of this exercise suggest the following: (1) based on the maximum residual offset believed to affect these measurements, local errors of no more than ± 20 K can be expected in these measurements due to registration error; (2) looking solely at the PDF distribution of the temperature field does not offer a complete view of the issue, but information about the spatial distribution has to be considered as well (possibly in relation to the effective spatial resolution offered by the measurements relative to the scales of the flow responsible for spatial variations, i.e., gradients); and (3) although the relative error is somewhat limited (on the order of a few percent), the actual spatial distribution of the temperature field can significantly be altered by erroneously enhancing spatial features of the flow. A complementary view to assess the impact of registration error is to consider the spatial temperature gradients directly. However, as described previously, these measurements are of somewhat limited SNR, which implies that (without any low-pass spatial filtering) the computation of gradients would be dominated by noise. Differentiating between errors in the gradients due to noise and due to registration errors would therefore be difficult from the measurements themselves (the objective in this work was to smooth the data as little as possible). To assess registration error limitations from this perspective free of limitations associated with noise, a similar analysis was extended to synthetic fields constructed from LES computations of a transverse jet in supersonic crossflow.

The LES computations of Kawai and Lele [32] were adapted and used to construct the necessary synthetic

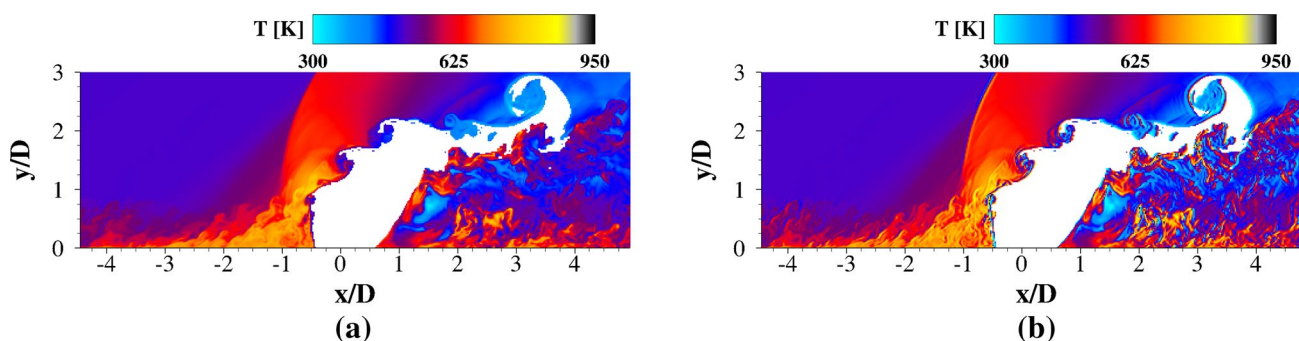


Fig. 14 Instantaneous temperature distribution from LES data: **a** true distribution, **b** PLIF thermometry reconstructed after shifting the views by 0.5 px. Original LES data from [32]

fields. Their LES computations are based on the experiments of [42] and consider an underexpanded sonic air jet injected into a Mach 1.6 air crossflow. The corresponding momentum flux ratio is $J = 1.7$. In the original experiment and in the LES calculations, the crossflow stagnation temperature was near room temperature, thus the range of flow temperature observed around the transverse jet are below room temperature. This was a major difference between their work and our configuration, and this range of temperature is outside the range of validity of the thermometry technique. To overcome these limitations, the temperature field obtained from the LES computation was rescaled to a freestream temperature of 500 K (rescaling was done equally throughout the domain). Although the rescaling still does not exactly match our configuration and makes the resulting field somewhat unphysical, for the purpose of replicating the experiment and assessing the impact of registration errors, this approach is expected to be adequate.

The experimental results were replicated by first selecting the center plane of the LES domain, then extracting the temperature, pressure and mixture fraction (based on jet fluid), and then using these two quantities to construct synthetic red and blue PLIF images via the model discussed previously. Note that a second significant difference in their setup is that toluene was not present in their flow. Thus, to construct the synthetic images, it was assumed that the crossflow fluid did passively carry the tracer by an arbitrary amount (here taken to be 0.5 % by volume—but this detail is actually inconsequential). No oxygen quenching was included in the analysis. Once the synthetic PLIF image pair was constructed, the rest of the procedure used to reconstruct the temperature field from the experiment was followed, including the addition of an artificial offset between the two views as done to construct Fig. 12, for example.

Figure 14 shows examples of the temperature field reconstructed from the LES synthetic PLIF images assuming (a) no offset, and (b) a residual offset of 0.5 pixel (the

masked-out portion corresponds to the same area masked-out in the actual experiments). The case with no offset is identical to the true temperature field. An offset of 0.5 pixel used to construct Fig. 14b is a relatively large amount, and it was selected to emphasize the artifacts introduced by the offset. The two views are qualitatively similar and show a somewhat similar range of temperature distribution. The general large-scale structures of the flow are also similar. However, the case with an offset gives a view of the smaller features of the flow with an enhanced but erroneous, contrast.

Using the reconstructed temperature field, temperature errors were inferred for different amounts of offset and are shown in Fig. 15. Figure 15a shows PDFs of the reconstructed temperature for different amounts of offset ranging from no offset (true solution), to 5 pixel. For this case, the PDF for an offset of 0.1 pixel is nearly identical to the true PDF. As the offset increases, the high- and low-temperature limits broaden over the true distribution. As observed from the experimental data, for sufficiently large values of offset, the PDF seems to approach a limiting profile. Positive and negative offsets result in the same PDF profile. Figure 15b shows PDFs of the error in reconstructed temperature (defined as the difference relative to the true solution). For a small offset (i.e., 0.1 pixel), the range of temperature error is generally small, with most probable errors only in the range of 10 K, but as the offset becomes significant, large errors can quickly arise. Furthermore, as the amount of offset increases (here at 5 pixel—which is probably an unrealistically large value) the tails of the distribution approach a limiting distribution and a small but systematic, error arises, as the second peak in the negative quadrant suggests.

Figure 15c shows PDFs of the (normalized) streamwise temperature gradient computed for the reconstructed field for different amounts of offset. Normalization was done by the scale T_a/D . The true solution is also shown for comparison. As was observed for the PDF of the temperature

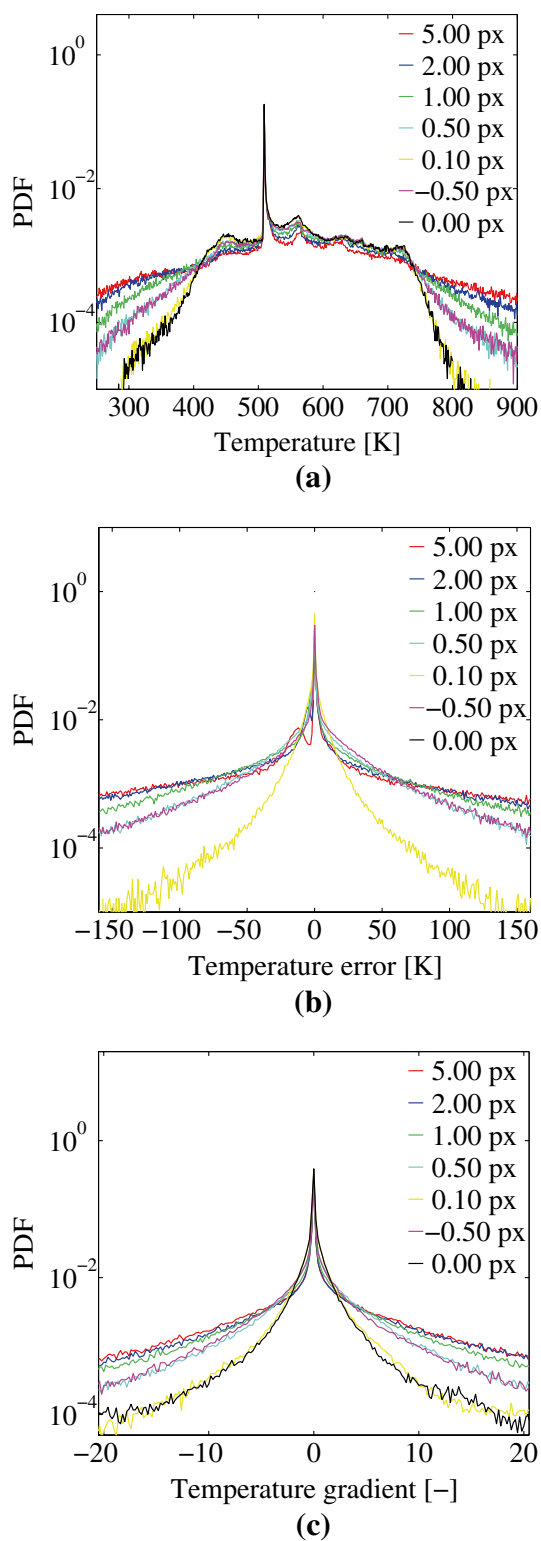


Fig. 15 PDF distribution of **a** instantaneous temperature, **b** temperature error, and **c** (normalized) temperature (streamwise) gradient, $(\partial T/\partial x)/(T_a/D)$, as a function of different imposed streamwise shifts between the BP280 and WG305 views

error, there is no practical difference between the temperature gradient extracted from the true and reconstructed temperature field with relative offsets of order 0.1 pixel. As the offset increases above this value, large differences between PDF curves can be observed. In particular, the probability to observe large temperature gradients increases substantially. This is consistent with the qualitative observation made from the reconstructed temperature of Figs. 12 and 14.

Finally, to further assess the dependence of reconstructed temperature error on the local spatial variation, joint PDFs between temperature, temperature gradients and their errors were computed and compared (not shown). Joint PDFs between the true local instantaneous temperature (streamwise) gradient and the temperature error show that for low offsets (of order 0.1 pixel), there is a strong correlation between temperature gradient and temperature error, while the correlation decreases as the amount of offset is increased. Particularly, for offsets larger than 1 pixel, no correlation exists and large errors can be encountered across all range of gradients. This is consistent with the qualitative observation of the imaging results. On the other hand, no significant correlation between true temperature gradient and gradient of the reconstructed temperature was observed.

6 Summary and conclusions

In this work, we have evaluated the performance of the single-excitation, dual-band-collection scheme of toluene laser-induced fluorescence used for temperature measurements in complex supersonic flows dominated by shock waves and characterized by non-uniform (mixing) flowfields. In particular, we considered transverse jets in supersonic crossflow where (room temperature) fluids with different molecular weight were injected into a moderate temperature (about 460 K) Mach 2.3 supersonic crossflow of toluene-seeded nitrogen that was generated by an expansion tube. A limited amount of work was also conducted to evaluate the feasibility of the thermometry technique in the presence of oxygen when air was used as the injection fluid. The technique is based on a ratiometric approach between simultaneous images taken over different spectral regions of the fluorescence spectrum and the temperature-induced red shift of toluene fluorescence. As a result, a calibration-free temperature-to-LIF ratio curve is constructed that is independent of pressure and composition. Seeding of the crossflow was quite effective in visualizing the structure of the full flowfield around the JISCF.

Owing to the strong temperature sensitivity, minute variation in the temperature field (due to mixing or compressibility effects) could be detected—see Fig. 2b where temperature variation due to acoustic waves emanating outward from the jet's shear layer could even be visualized. We constructed (Sect. 5.1) a zero-dimensional mixing model to describe the LIF signal arising from isobaric mixing between a cold fluid and toluene-seeded hot fluid. We found that the LIF signal is a non-monotonic function of mixture fraction ζ . In particular, it shows a maximum at some intermediate value of ζ (see Fig. 7b). This non-monotonic dependence is the result of the competing effect of tracer dilution (which linearly depends on ζ —i.e., the tracer number density linearly decreases with ζ) and the exponential sensitivity to temperature (the FQY exponentially increase as temperature decrease—i.e., as ζ increases in our simple model). It has to be pointed out that this effect is expected to occur also for other tracers, for example acetone. However, because of the strong temperature sensitivity of toluene LIF, this effect is particularly strong in this case. This property can be exploited to identify regions where mixing occurs, such as the formation of the windward shear (mixing) layer of the JISCF.

Using this method, we were able to extract local measurements of temperature, (freestream normalized) number density and partial pressure. These quantities are used as a proxy for scalar mixing. Analysis of the accuracy of the measured quantities was performed. PDF distributions of the measured temperature show a peak value near at 460 K, which matches the value of the freestream temperature inferred by other means [26], thus reinforcing that the method is capable of providing accurate measurements without complex in-situ calibration steps. Estimates of the SNR were used as a metric to assess the precision of the measurements. In particular, SNR of temperature computed spatially suggests that SNR values in the range 30 to 50 can be obtained in uniform regions (e.g., the freestream), while SNR values of order 20 are found in the wake of the transverse jet. However, the temperature field in the wake is non-uniform because of the ongoing turbulent mixing; therefore, the SNR computed here is also limited by spatial variations associated with the flow non-uniformity and it might thus be underestimated. The SNR values for the reconstructed number density and partial pressure are only of order 5, however. In spite of the somewhat limited SNR, the spatial distribution of temperature, number density and partial pressure provide a valuable representation of the overall structure and mixing properties of the system.

A few experiments were also conducted with air injection to investigate the impact of oxygen quenching on these measurements. Although acceptable quality LIF images can be acquired, the SNR values of the reconstructed temperature suffer significantly. Part of the limitation arises

from the low LIF signal in the region where mixing occurs, but part of it is that air injection (similarly to nitrogen and argon injection) was found to produce fluid dynamically non-uniform flows due to the nature of the rapid mixing, which then impacts the assessment of the SNR even further. In any case, it seems that it is also possible to use the technique to extract valuable temperature measurements even with air. One main limitation is that reconstruction of the number density is not directly possible when oxygen quenching is present.

One key but subtle, challenge was associated with registration errors in matching the blue and red views to compute the LIF ratio and thus the local temperature. This is a limitation that is shared among any ratiometric-based technique and it is rendered more difficult in cases with strong flow non-uniformities. Numerical experiments were used to investigate shifts between PLIF images on the resulting temperature field. The analysis shows that regions of large spatial variations are affected in a manner to bias the measured temperature to higher values, and to skew the spatial structure of the temperature field such that the local spatial gradients of temperature are overestimated. The amount of distortion is found to depend on the amount of offset. Although the resulting error in the temperature field is somewhat limited, the spatial structure is greatly distorted even for spatial offsets of order of half pixel. Relative offsets less than 0.1 pixel (which can be obtained in practice) result in local temperature errors estimated to be at worst ± 20 K, but with a more significant impact on the accuracy of spatial gradients. For low value of offset (up to a few tenths of pixel), a well-defined correlation between temperature errors and (true) spatial gradients was found (not shown), while for larger offsets, the correlation diminished and disappeared.

The error assessment associated with image registration has been quantified here in terms of pixel offset only. Because the amount of error depends on the local spatial variability of the property being measured (e.g., local gradient), perhaps a more relevant approach would be to identify the amount of offset in pixel units that can be tolerated based on a measure of the spatial resolution of the measurements. For example, it seems reasonable that the ratio between a flow scale responsible for flow non-uniformity and the resolving power of the imaging system (projected pixel size or effective imaging resolution of the whole system) should be the relevant quantity to determine what would be the impact of a given amount of offset on the accuracy of the measured local temperature and other quantities. Therefore, in considering the results of this and similar studies, this aspect should be taken into consideration and could be an opportunity for a more refined optimization of the method. However, many experiments, including the current one, might effectively be under-resolved,

which means that the image discretization (pixel dimension combined with resolving power of the imaging system) is the only limiting length scale that acts as a low-pass spatial filtering operation, therefore limiting the detected spatial variation of the field being measured. In this context, the results of the analysis presented here on registration errors given in terms of pixel units can therefore be sufficient and provide some practical guidance for cases other than this specific study.

Acknowledgments This paper is based on work supported by the Department of Energy sponsored Predictive Science Academic Alliance Program (PSAAP) Center at Stanford University under award number DE-FC52-08NA28614. This work was also partially supported by the Air Force Office of Scientific Research (AFOSR) with Dr. Julian Tishkoff as technical monitor. The authors would also like to thank Jon Koch, Wieland Koban, and Christof Schulz for the toluene fluorescence spectra data they graciously provided. Additionally, Victor A. Miller is supported by the Claudia and William Coleman Foundation Stanford Graduate Fellowship.

References

1. C. Schulz, V. Sick, Tracer-lif diagnostics: quantitative measurement of fuel concentration, temperature and fuel/air ratio in practical combustion systems. *Prog. Energy Combust. Sci.* **31**(1), 75–121 (2005)
2. J.D. Koch, R.K. Hanson, W. Koban, C. Schulz, Rayleigh-calibrated fluorescence quantum yield measurements of acetone and 3-pentanone. *Appl. Opt.* **43**(31), 5901–5910 (2004)
3. A. Lozano, B. Yip, R.K. Hanson, Acetone: a tracer for concentration measurements in gaseous flows by planar laser induced fluorescence. *Exp. Fluids* **13**(6), 369–376 (1992)
4. C. Combs, N.T. Clemens, Measurements of ablation-products transport in a mach 5 turbulent boundary layer using naphthalene PLIF, in *53rd AIAA Aerospace Sciences Meeting, American Institute of Aeronautics and Astronautics (AIAA)*, (2015). doi:10.2514/6.2015-1912
5. C. Combs, N.T. Clemens, P.M. Danehy, Development of naphthalene PLIF for visualizing ablation products from a space capsule heat shield, in *52nd Aerospace Sciences Meeting, American Institute of Aeronautics and Astronautics (AIAA)*, (2014). doi:10.2514/6.2014-1152
6. V. Narayanaswamy, R. Burns, N.T. Clemens, Kr-PLIF for scalar imaging in supersonic flows. *Opt. Lett.* **36**(21), 4185 (2011). doi:10.1364/ol.36.004185
7. J. Trost, L. Zigan, A. Leipertz, D. Sahoo, P.C. Miles, Fuel concentration imaging inside an optically accessible diesel engine using 1-methylnaphthalene planar laser-induced fluorescence. *Int. J. Eng. Res.* **15**(6), 741–750 (2014). doi:10.1177/1468087413515658
8. S. Faust, M. Goschütz, S.A. Kaiser, T. Dreier, C. Schulz, A comparison of selected organic tracers for quantitative scalar imaging in the gas phase via laser-induced fluorescence. *Appl. Phys. B* **117**(1), 183–194 (2014). doi:10.1007/s00340-014-5818-x
9. S. Faust, G. Tea, T. Dreizer, C. Schultz, Temperature, pressure and bath gas composition dependence on fluorescence spectra and fluorescence lifetimes of toluene and naphthalene. *Appl. Phys. B: Lasers Opt.* **110**, 81–93 (2013)
10. W. Koban, Photophysical characterization of toluene and 3-pentanone for quantitative imaging of fuel/air ratio and temperature in combustion systems. Ph.D. thesis, University of Heidelberg (2005)
11. W. Koban, J.D. Koch, R.K. Hanson, C. Schulz, Absorption and fluorescence of toluene vapor at elevated temperatures. *PCP* **6**, 2940–2945 (2004)
12. W. Koban, J.D. Koch, R.K. Hanson, C. Schulz, Toluene LIF at elevated temperatures: implications for fuel–air ratio measurements. *Appl. Phys. B: Lasers Opt.* **80**, 147–150 (2005b)
13. J. Koch, Fuel Tracer Photophysics for Quantitative Planar Laser-Induced Fluorescence. Ph.D. thesis, Stanford University (2005)
14. M. Cundy, P. Trunk, A. Dreizler, V. Sick, Gas-phase toluene LIF temperature imaging near surfaces at 10 khz. *Exps. Fluids* **51**(5), 1169–1176 (2011)
15. W. Koban, J.D. Koch, V. Sick, N. Wermuth, R.K. Hanson, C. Schulz, Predicting lif signal strength for toluene and 3-pentanone under engine-related temperature and pressure conditions, in *Proceedings of the Combustion Institution*, vol 30, pp 1545–1553, (2005)
16. M. Luong, R. Zhang, C. Schulz, V. Sick, Toluene laser-induced fluorescence for in-cylinder temperature imaging in internal combustion engines. *Appl. Phys. B: Lasers Opt.* **91**, 669–675 (2008)
17. B. Peterson, E. Baum, B. Bohm, V. Sick, A. Dreizler, Evaluation of toluene lif thermometry detection strategies applied in an internal combustion engine. *Appl. Phys. B: Lasers Opt.* **117**(1), 151–175 (2014)
18. W. Koban, J.D. Koch, R.K. Hanson, C. Schulz, Oxygen quenching of toluene fluorescence at elevated temperatures. *Appl. Phys. B: Lasers Opt.* **80**, 777–784 (2005a)
19. J. Reboux, D. Puechberty, F. Dionnet, A new approach of plif applied to fuel/air ratio measurement in the compression stroke of an optical si engine, in *SAE technical paper series No. 941988*, (1994)
20. B. Cheung, Tracer-based planar laser-induced fluorescence diagnostics: quantitative photophysics and time-resolved imaging. Ph.D. thesis, Stanford University (2011)
21. J. Yoo, Strategies for Planar Laser-Induced Fluorescence Thermometry in Shock Tube Flows. Ph.D. thesis, Stanford University (2011)
22. K. Mohri, M. Luong, G. Vanhove, T. Dreier, C. Schulz, Imaging of the oxygen distribution in an isothermal turbulent free jet using two-color toluene LIF imaging. *Appl. Phys. B: Lasers Opt.* **103**(3), 707–715 (2011)
23. W. Koban, J. Schorr, C. Schulz, Oxygen-distribution imaging with a novel two-tracer laser-induced fluorescence. *Appl. Phys. B: Lasers Opt.* **74**, 111–114 (2002)
24. V.A. Miller, V.A. Troutman, M.G. Mungal, R.K. Hanson, 20 kHz toluene planar laser-induced fluorescence imaging of a jet in nearly sonic crossflow. *Appl. Phys. B: Lasers Opt.* **117**(1), 401–410 (2014)
25. S. Kaiser, M. Schild, C. Schulz, Thermal stratification in an internal combustion engine due to wall heat transfer measured by laser-induced fluorescence. *Proc. Combust. Inst.* **34**, 2911–2919 (2013)
26. V.A. Miller, M. Gamba, M.G. Mungal, R.K. Hanson, Single- and dual-band collection toluene PLIF thermometry in supersonic flows. *Exp. Fluids* **54**, 1539 (2013)
27. B. Peterson, E. Baum, B. Bohm, V. Sick, A. Dreizler, High-speed piv and lif imaging of temperature stratification in an internal combustion engine. *Proc. Combust. Inst.* **34**, 3653–3660 (2013)
28. J. Yoo, D. Mitchell, D. Davidson, R.K. Hanson, Planar laser-induced fluorescence imaging in shock tube flows. *Exp. Fluids* **45**, 751–759 (2010)
29. J. Yoo, D. Mitchell, D. Davidson, R.K. Hanson, Near-wall imaging using toluene-based planar laser-induced fluorescence in shock tube flow. *Shock Waves* **21**, 523–532 (2011)

30. A.R. Karagozian, Transverse jets and their control. *Prog. Energy Combust. Sci.* **36**(5), 531–553 (2010)
31. K. Mahesh, The interaction of jets with crossflow. *Annu. Rev. Fluid Mech.* **45**, 379–407 (2013)
32. S. Kawai, S.K. Lele, Large-eddy simulation of jet mixing in supersonic crossflows. *AIAA J.* **48**(9), 2063–2083 (2010)
33. W. Koban, Private communication (2012)
34. W.N. Heltsley, J.A. Snyder, A.J. Houle, D. Davidson, M.G. Mungal, R.K. Hanson, Design and characterization of the Stanford 6 inch expansion tube, in *42nd AIAA/ASME/SAE/ASEE Joint Propulsion Conference & Exhibit*, 9–12 July, AIAA-2006-4443 (2006)
35. V.A. Miller, High-Speed Tracer-Based PLIF Imaging for Scramjet Ground Testing. Ph.D. thesis, Stanford University (2014)
36. R.L. Trimpi, A preliminary theoretical study of the expansion tube, a new device for producing high-enthalpy short-duration hypersonic gas flows. Tech. Rep. NASA TR R-133 (1962)
37. N.T. Clemens, Flow imaging, in *Encyclopedia of Imaging Science and Technology* (Wiley, 2002)
38. J. Davitian, D.R. Getsinger, C. Hendrickson, A.R. Karagozian, Transition to global instability in transverse-jet shear layers. *J. Fluid Mech.* **661**, 294–315 (2010)
39. D.R. Getsinger, C. Hendrickson, A.R. Karagozian, Shear layer instabilities in low-density transverse jets. *Exp. Fluids* **53**, 783–801 (2012)
40. D.E. Everett, M.A. Woodmansee, J.C. Dutton, M.J. Morris, Wall pressure measurements for a sonic jet injected transversely into a supersonic crossflow. *J. Propul. Power* **14**(6), 861–868 (1998)
41. M.R. Gruber, L.P. Goss, Surface pressure measurements in supersonic transverse injection flowfields. *J. Propul. Power.* **15**(5), 633–641 (1999)
42. J.G. Santiago, J.C. Dutton, Velocity measurements of a jet injected into a supersonic crossflow. *J. Propul. Power.* **13**(2), 264–273 (1997)